catalysts

MDPI

Article

The Property–Efficiency Relationship over Rh/Ga_xNb_y Catalysts in Photothermal Dry Reforming of CH_4

Yuqiao Li [1,†], Shaoyuan Sun [1,†], Dezheng Li [1,†], Huimin Liu [1,*] and Yiming Lei [1,2,*]

[1] School of Chemical and Environmental Engineering, Liaoning University of Technology, Jinzhou 121001, China; yuqiao.li@njust.edu.cn (Y.L.); ssy231882008@163.com (S.S.); ldz221882002@163.com (D.L.)
[2] Departament de Química (Unitat de Química Inorgànica), Facultat de Ciències, Universitat Autònoma de Barcelona (UAB), Cerdanyola del Valles, 08193 Barcelona, Spain
* Correspondence: liuhuimin08@tsinghua.org.cn (H.L.); 1689472@uab.cat (Y.L.)
† These authors contributed equally to this work.

Abstract: Photothermal catalytic dry reforming of methane (DRM) technology not only achieves artificial photosynthesis of fuels but also decreases greenhouse effects. The highly efficient photothermal DRM reaction depends on elaborate catalysts. Therefore, unraveling the relationship between property and catalytic efficiency of catalysts is crucial. In this study, a series of Rh-loaded Ga_2O_3-Nb_2O_5 (Rh/Ga_xNb_y) were designed via a simple in situ reduction strategy using Rh_2O_3/Ga_2O_3-Nb_2O_5 as a precursor. After an accurate material characterization, as a proof-of-principle, the photothermal efficiency could be attributed to (i) the amount of medium and strong basic sites on the catalyst surface; (ii) the number of electron–hole pairs upon visible light irradiation. Accordingly, this study used Rh/Ga_xNb_y as a model hybrid catalyst to clarify the relationship between the fundamental properties and photothermal catalytic DRM activities, thus providing guidance for the rational design and fabrication of efficient metal/semiconductor composite catalysts for DRM implementation.

Keywords: dry reforming of CH_4; photothermal catalyst; property–efficiency relationship; Rh-based catalyst; composite catalyst

Academic Editor: Concetta Ruocco

Received: 13 February 2025
Revised: 17 March 2025
Accepted: 19 March 2025
Published: 25 March 2025

Citation: Li, Y.; Sun, S.; Li, D.; Liu, H.; Lei, Y. The Property–Efficiency Relationship over Rh/Ga_xNb_y Catalysts in Photothermal Dry Reforming of CH_4. *Catalysts* **2025**, *15*, 312. https://doi.org/10.3390/catal15040312

1. Introduction

Dry reforming of methane (DRM) is a promising strategy to solve the greenhouse effect, which is one of the most severe environmental challenges [1,2]. DRM technology converts two greenhouse gases (CO_2 and CH_4) into high-value-added syngas (CO and H_2), which can be further utilized in downstream chemical reactions [3,4]. Most of the industrialized DRM is driven by heat in the thermal catalytic DRM reaction; however, the thermal-driven DRM process requires high reaction temperatures, inevitably leading to excessive energy consumption and catalyst inactivation [5,6]. In order to deal with the main challenges in conventional thermal catalytic DRM systems, introducing sustainable solar light energy to induce the photothermal catalytic DRM reaction is attracting more and more attention because photothermal catalysis can effectively achieve the conversion of CO_2 and CH_4 into syngas under mild conditions, which is beneficial for alleviating the greenhouse effect and achieving carbon neutrality goals.

The DRM reaction is typically conducted at high temperatures (700–900 °C) to achieve high conversion rates of CH_4 and CO_2, as well as to minimize coke formation. However, operating at such high temperatures poses significant challenges, including high

energy consumption, catalyst sintering, and increased operational costs [7]. In recent years, there has been growing interest in developing DRM catalysts that can operate at lower temperatures (500–600 °C) to address these challenges [8]. Lower-temperature DRM not only reduces energy requirements but also opens up opportunities for integrating DRM with other processes, such as photothermal catalysis, which can further enhance reaction efficiency under mild conditions.

To date, multiple catalysts like noble metal-, transition metal-, and metal oxide-based catalysts have been designed and developed for photothermal DRM applications. For instance, Cho et al. used the hydrothermal method to load Rh nanoparticles (Rh-NPs) onto TaON and tested the photocatalytic activity of the Rh/TaON catalyst in photothermal DRM. The results demonstrated that the catalytic activity of Rh/TaON under light assistance was much higher than that achieved under the traditional thermal-driven catalytic system [9]. Wang et al. prepared a supported Ni-Si/ZrO_2 catalyst using the impregnation method, which exhibited high activity for DRM at 400 °C, recording initial CH_4 and CO_2 conversion rates of 0.50 s^{-1} and 0.44 s^{-1}, respectively [10]. In addition, the moderate interaction between ZrO_2 and Ni promoted the formation of small Ni-NPs (6–9 nm) with strong electron donor ability, which maintained the Ni metallic state under reaction conditions, reducing catalyst deactivation. Ye group's studies revealed that bimetallic catalysts, consisting of one active metal for thermal-driven DRM and one plasmonic metal, such as RhAu/SiO_2 [11], PtAu/SiO_2 [12], and PdAu/Al_2O_3 [13], could realize high activities for DRM under visible light irradiation. Hou et al. prepared several noble (Ru, Rh, Pt, Pd, and Ir at 5 wt% metal load) and transition (Ni and Co at 10 wt% metal load) metal-based catalysts (supported on Al_2O_3) and evaluated their activity on the dry reforming of methane with CO_2 [14]. Hassan et al. evaluated the catalytic activity of non-porous and mesoporous (SBA-15) silica supports (SiO_2) impregnated with cobalt (12 wt%) and small amounts of rhodium (0.2 and 0.5 wt%) [15]. Recently, our group designed efficient Rh-based photothermal catalysts for photothermal DRM, showing excellent catalytic activity under mild reaction conditions and confirming the great potential of photothermal effect in improving DRM efficiency [16]. These works suggested that some reducible oxides, such as WO_3, Nb_2O_5, and Ga_2O_5, which support group VIII metal catalysts, could be partially reduced in situ during the DRM reaction [17,18]. The in situ-generated group VIII metal NPs served as the active sites for DRM. On the other hand, the partially reduced supports with oxygen vacancies enhanced the visible light harvesting capacities, which further introduces a photothermal mechanism into the DRM process for improving catalytic activities. Considering the advantages of photothermal composite catalysts including group VIII metals and reducible oxide supports, it is necessary to further elucidate the relationship between their fundamental properties and catalytic DRM efficiency, paving the way for reasonably designed highly efficient catalysts.

Motivated by the aforementioned necessity and benefit, in this study, an Rh-loaded Ga_2O_{3-x}-Nb_2O_{5-x} (Rh/Ga_xNb_y) photothermal catalytic system was constructed via a straightforward in situ reduction method and used as a model catalyst to investigate the property–activity relationship during the DRM process. The Rh/Ga_xNb_y catalysts were fabricated by (i) physically mixing Ga_2O_3 and Nb_2O_5 to obtain Ga_2O_3-Nb_2O_5 support; (ii) loading Rh_2O_3 onto Ga_2O_3-Nb_2O_5 via an impregnation method; and (iii) in situ reduction of the Rh_2O_3/Ga_2O_3-Nb_2O_5 precursor during the DRM process to prepare a Rh/Ga_xNb_y photothermal catalyst. The properties of the as-prepared catalysts were systematically characterized by XRD, BET, CO_2-TPD, and UV-vis, as well as photoelectrochemical analysis. Then, the catalytic DRM efficiency of Rh/Ga_xNb_y was evaluated under the traditional thermal-driven and photothermal catalytic system. The improvement effect of photothermal catalytic DRM efficiency should be mainly accounted for by the abundant active sites and photoexcited charge carriers. This work not only designs a highly efficient

photothermal catalyst via a simple in situ reduction strategy but also provides guidance for a rational catalyst design by clarifying the relationship between basic properties and DRM catalytic behaviors.

2. Results and Discussion

2.1. Catalyst Synthesis and Characterization

As shown in the experimental section, the Rh_2O_3/Ga_2O_3-Nb_2O_5 precursor was obtained by straightforward physical mixing of Ga_2O_3-Nb_2O_5 and impregnation treatment for 12 h. Subsequently, the Rh/Ga_xNb_y catalysts were prepared by an in situ reduction method under 10% H_2/Ar at 500 °C for 2 h, which used Rh_2O_3/Ga_2O_3-Nb_2O_5 as a precursor.

In order to check whether Rh_2O_3/Ga_2O_3-Nb_2O_5 could be in situ-reduced in the DRM process, H_2-TPR characterizations were conducted over Rh_2O_3/Ga_2O_3-Nb_2O_5 and Ga_2O_3-Nb_2O_5. As shown in Figure 1a, there were roughly two reduction peaks over each Rh_2O_3/Ga_2O_3-Nb_2O_5 precursor when temperatures were lower than 500 °C. The peak centered at ~140 °C corresponded to the reduction of Rh_2O_3 to metallic Rh [19,20]. On the other hand, since both Ga_2O_3 and Nb_2O_5 could be partially reduced by H_2 at temperatures lower than 460 °C according to literature reports [18], the peak in the range of 300–460 °C might be due to the partial reduction of Ga_2O_3-Nb_2O_5 support. In Figure S1, the H_2-TPR results of the Ga_2O_3-Nb_2O_5 precursors show no obvious peak in the range of 300–460 °C, suggesting the characteristic peaks should be due to the partial reduction of Ga_2O_3-Nb_2O_5. The H_2-TPR results were consistent with our previous studies, which demonstrated that Rh_2O_3-Nb_2O_5 and Rh_2O_3-Ga_2O_3 could be reduced in situ in the DRM reaction [16,18].

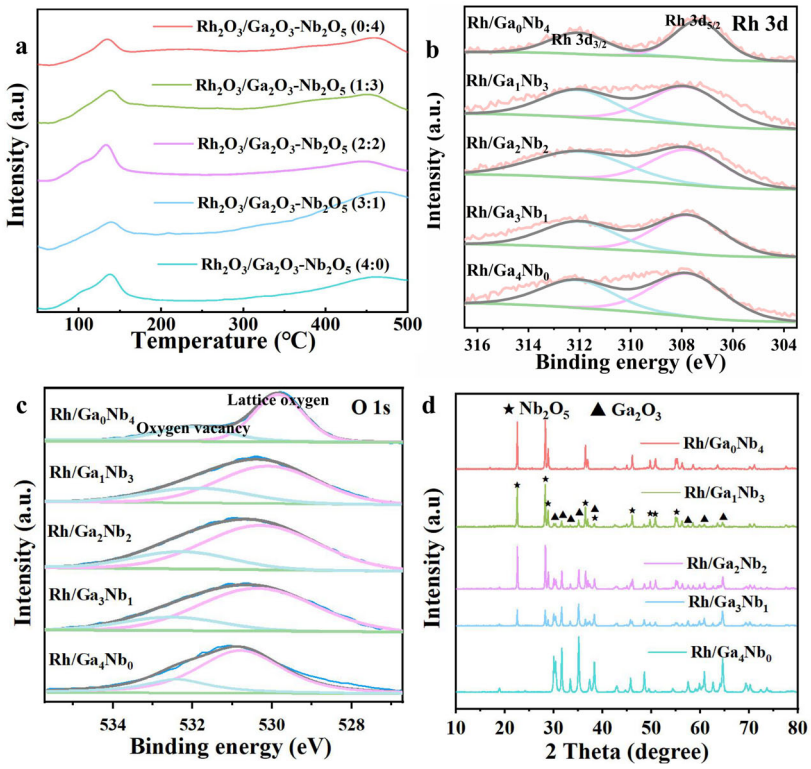

Figure 1. (**a**) The H_2-TPR results of Rh_2O_3/Ga_2O_3-Nb_2O_5 precursors. XPS spectra of (**b**) Rh 3d and (**c**) O 1s in the spent Rh/Ga_xNb_y catalysts. (**d**) XRD patterns of Rh/Ga_xNb_y catalysts.

The valence states of Rh and O on the spent catalysts were characterized by XPS. According to the Rh 3d spectra (Figure 1b), two peaks with binding energies of 307.8 eV and 312.2 eV could be observed, corresponding to Rh $3d_{5/2}$ and Rh $3d_{3/2}$, respectively [21,22]. This result indicated that Rh_2O_3 on Rh_2O_3/Ga_2O_3-Nb_2O_5 was reduced to metallic Rh. In

Figure 1c, two peaks centered at binding energies of 531.7–532.5 eV and 529.3–530.7 eV were detected, which belong to oxygen vacancies and lattice oxygen, respectively [23,24]. The existence of oxygen vacancies indicated that Ga_2O_3-Nb_2O_5 precursors were in situ-reduced in DRM. This phenomenon could be attributed to the interaction between Ga and oxygen vacancies, which altered the electronic state around the vacancies. The increase in Ga content changes the charge density around the oxygen vacancies, affecting the local electronic environment. This modification in charge distribution could result in an increase in the binding energy of the electron states related to oxygen vacancies, leading to the observed peak shift in the XPS spectrum. The contents of oxygen vacancies and lattice oxygen on the spent catalysts were further calculated, as shown in Table 1. The contents of oxygen vacancies on the spent catalysts increased with the increase in the Nb_2O_5 portion. The above results confirmed that Rh_2O_3/Ga_2O_3-Nb_2O_5 catalyst precursors were in situ-reduced in the DRM reaction. H_2-TPR characterization and XPS analysis indicated that Rh-NPs were in situ-formed during the initial stage of the DRM reaction since Rh_2O_3 can be reduced to metallic Rh-NPs at relatively low temperatures in a reductive atmosphere (the reductivity of CH_4 is strong and the oxidizing property of CO_2 is weak). According to previous reports [16,18], the Rh-NPs could serve as active sites, driving the DRM reaction to generate CO and H_2. Besides the reduced Rh-NPs, in the effluent of the DRM reaction, H_2 and other reductive gases (i.e., CO and CH_4) further partially reduce the Ga_2O_3-Nb_2O_5 supports.

Table 1. Amounts of lattice oxygen and oxygen vacancies in the Rh/Ga_xNb_y catalysts.

Spent Catalyst	Lattice Oxygen (%)	Oxygen Vacancy (%)
Rh/Ga_0Nb_4	70.6	29.4
Rh/Ga_1Nb_3	73.8	26.2
Rh/Ga_2Nb_2	75.6	24.4
Rh/Ga_3Nb_1	79.2	20.8
Rh/Ga_4Nb_0	79.5	20.5

After confirming the successful reduction of Rh_2O_3/Ga_2O_3-Nb_2O_5 to Rh/Ga_xNb_y, the following characterizations were conducted over Rh/Ga_xNb_y model catalysts to further investigate the property–efficiency relationship. The crystalline structures of Rh/Ga_xNb_y catalysts were characterized by XRD. As shown in Figure 1d, the peaks from Rh/Ga_4Nb_0 could be detected at 30.1°, 31.2°, 33.6°, 35.0°, 38.3°, 57.5°, 60.8°, and 64.9°, which were attributed to the crystal phase of β-Ga_2O_3 [25,26]. Over Rh/Ga_0Nb_4, the peaks located at 22.3°, 28.5°, 29.1°, 36.5°, 38.3°, 46.3°, 50.2°, 50.8°, and 55.2° could be assigned to orthorhombic Nb_2O_5 [27]. Regarding the Rh/Ga_xNb_y composite catalysts, the coexistence of characteristic peaks of both β-Ga_2O_3 and orthorhombic Nb_2O_5 indicated that the physical mixing did not change the crystal structure. The lack of Rh peaks in the XRD spectra of Rh/Ga_xNb_y catalysts should be attributed to the small sizes and low amount of Rh-NPs.

HR-TEM images of the Rh/Ga_xNb_y catalysts are displayed in Figures 2 and S2. As clearly shown in Figure 2b, Rh NPs with a size of 0.23 nm and lattice spacing of 0.38 nm belonging to the (040) plane of Nb_2O_5 were observed. Figure S2 shows the morphology of the Rh/Ga_1Nb_3, Rh/Ga_2Nb_2, Rh/Ga_3Nb_1, and Rh/Ga_4Nb_0 catalysts, indicating that Rh NPs were uniformly dispersed on the Ga_xNb_y substrate.

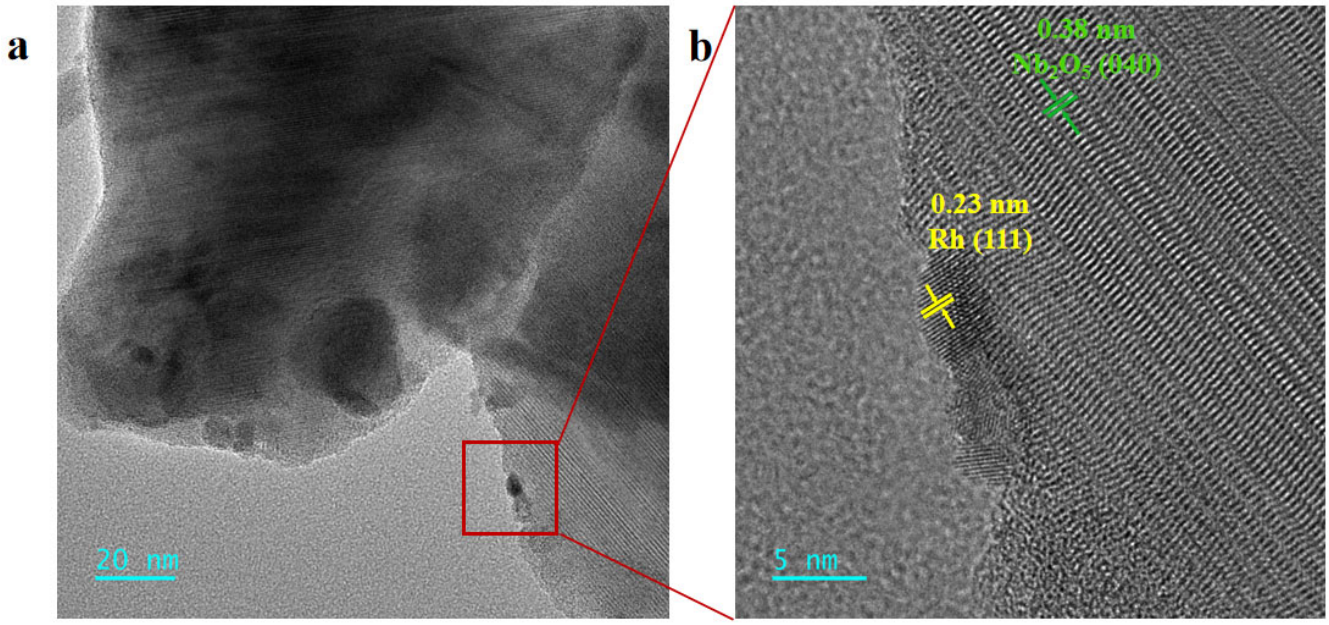

Figure 2. (**a**) TEM and (**b**) HR-TEM images of Rh/Ga_0Nb_4.

BET characterization was conducted over the Rh/Ga_xNb_y catalysts. Figure 3a reveals that Nb_2O_5, Ga_2O_3, and all the catalysts exhibited the IV-type adsorption–desorption isotherms with an H3 hysteresis loop, indicating that the pores over the catalysts were mainly in the form of narrow slits [28,29]. As shown in Table 2, the specific surface areas of Nb_2O_5 and Ga_2O_3 were very small (3.9–5.3 $m^2\ g^{-1}$), and the average pore sizes were 19.1–21.6 nm. The physical mixing of Nb_2O_5 and Ga_2O_3 as well as the loading of Rh onto the supports did not alter the specific surface areas and average pore sizes significantly, with the specific surface areas of the Rh/Ga_xNb_y catalysts in the range of 3.3–6.3 $m^2\ g^{-1}$ and the average pore sizes in the range of 14.8–28.0 nm.

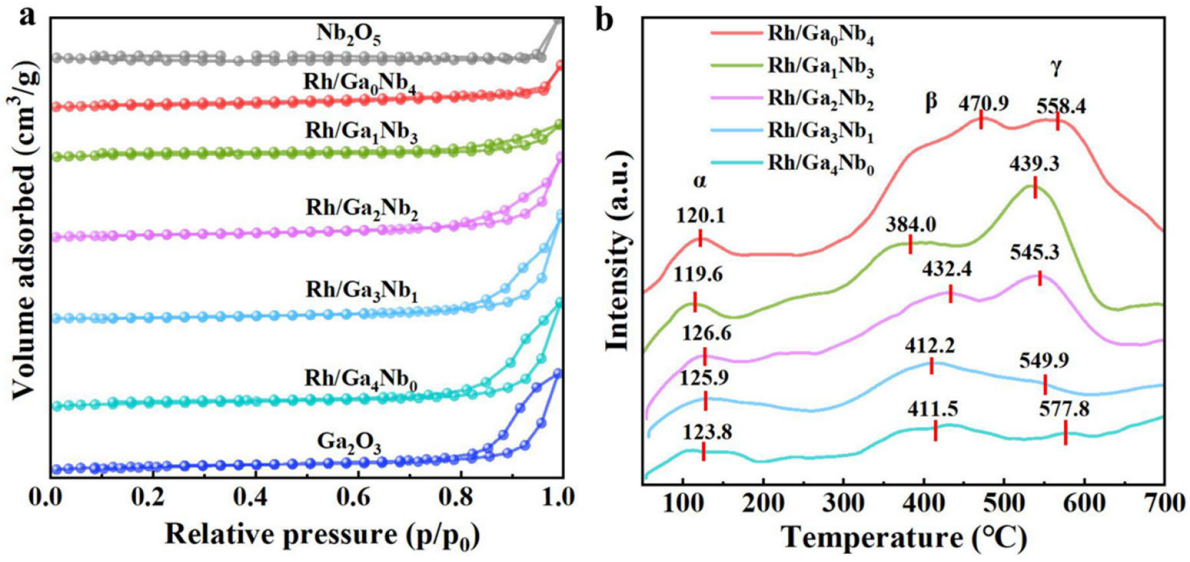

Figure 3. (**a**) N_2 adsorption–desorption isotherms of the Rh/Ga_xNb_y catalysts. (**b**) CO_2-TPD profiles of the Rh/Ga_xNb_y catalysts.

Table 2. Specific surface area and average pore size of Nb_2O_5, Ga_2O_3, and Rh/Ga_xNb_y.

Catalyst	Specific Surface Area ($m^2 \cdot g^{-1}$)	Average Pore Size (nm)
Nb_2O_5	5.3	21.6
Rh/Ga_0Nb_4	6.3	23.6
Rh/Ga_1Nb_3	3.6	13.3
Rh/Ga_2Nb_2	4.7	21.4
Rh/Ga_3Nb_1	3.3	28.0
Rh/Ga_4Nb_0	3.3	14.8
Ga_2O_3	3.9	19.1

The results of CO_2-TPD characterization over the Rh/Ga_xNb_y catalysts are displayed in Figure 3b, showing three typical CO_2 desorption peaks. The peak at low temperatures (119.6–126.6 °C, denoted as α peak) belonged to the desorption of CO_2 at the weak basic adsorption site of the catalysts. The peaks located at 384.0–470.9 °C (designated as β peak) and 439.3–577.8 °C (noted as γ peak) were attributed to the CO_2 molecules' desorption from the medium and strong basic sites, respectively [30,31]. The medium and strong basic sites played important roles in improving the adsorption and activation of CO_2, through acid–base interactions [32,33]. Notably, Rh/Ga_0Nb_4 exhibited the strongest β and γ peaks, while the two peaks over the Rh/Ga_4Nb_0 catalyst were the weakest. Moreover, with the introduction of Nb_2O_5, the CO_2 desorption peaks of the Rh/Ga_xNb_y catalysts gradually strengthened. Quantitative analysis of the CO_2-TPD profiles in Table 3 reveals that compared to the Rh/Ga_4Nb_0 catalyst, the medium and strong basic sites over Rh/Ga_0Nb_4 and the other Rh/Ga_xNb_y catalysts were both increased, but the weak basic sites had only slight variation. As the amount of Nb_2O_5 increased, the number of medium and strong basic sites for CO_2 adsorption also increased, with the order of CO_2 adsorption ability as follows: Rh/Ga_0Nb_4 > Rh/Ga_1Nb_3 > Rh/Ga_2Nb_2 > Rh/Ga_3Nb_1 > Rh/Ga_4Nb_0.

Table 3. Quantitative analysis of CO_2-TPD results.

Catalyst	Amounts of CO_2 Desorption ($\mu mol \cdot g^{-1}$)			
	α	β	γ	β + γ
Rh/Ga_0Nb_4	3.42	25.9	27.7	53.6
Rh/Ga_1Nb_3	4.07	14.8	19.4	34.2
Rh/Ga_2Nb_2	3.0	12.4	16.0	28.4
Rh/Ga_3Nb_1	4.3	9.9	5.3	15.2
Rh/Ga_4Nb_0	2.4	7.9	3.5	11.4

The optical properties of the Nb_2O_5, Ga_2O_3, and Rh/Ga_xNb_y catalysts were characterized via UV-vis spectroscopy. Figures 4a and S3 show that Ga_2O_3 mainly absorbed UV light and Nb_2O_5 could absorb both UV light and visible light (λ < 420 nm). Tauc plots were obtained based on these absorption spectra, and the bandgaps were estimated as shown in Figure S4. The loading of Rh-NPs significantly enhances the visible light absorbance ability. In addition, compared to Rh/Ga_4Nb_0, the introduction of Nb_2O_5 also enhanced the visible light absorption capability of the Rh/Ga_xNb_y catalysts. With the increase in Nb_2O_5 content in the Rh/Ga_xNb_y catalysts, the light-harvesting capacity of the Rh/Ga_xNb_y catalysts also increased.

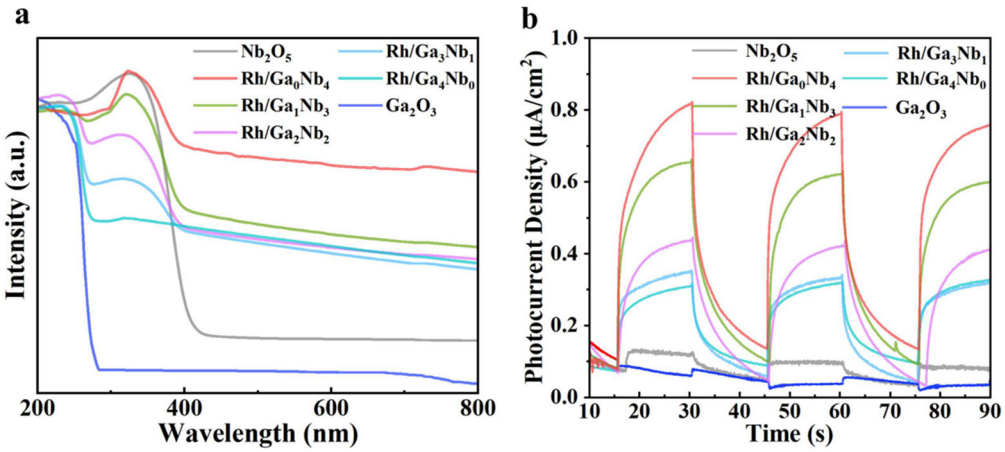

Figure 4. (**a**) UV-vis spectra of Rh/Ga_xNb_y catalysts. (**b**) Transient photocurrent of Rh/Ga_xNb_y catalysts under visible light irradiation.

The separation and transfer behavior of photogenerated electron–hole pairs over the Rh/Ga_xNb_y catalysts were characterized via photoelectrochemical current–time measurements. Figure 4b reveals that all the Rh/Ga_xNby catalysts had a rapid photocurrent response when exposed to light illumination. The photocurrent intensity of the Rh/Ga_xNb_y catalysts increased with the proportion of Nb_2O_5. Compared to the Nb_2O_5 and Ga_2O_3 support, the photocurrent intensity of the Rh-loaded catalysts increased, indicating that the introduction of Rh and Nb_2O_5 improved the amount and transfer of charge carriers.

2.2. Catalytic Efficiency Evaluation in DRM

Having investigated the fundamental properties of the catalytic DRM activities of the Rh/Ga_xNb_y catalysts, they were evaluated under thermal (500 °C) or photothermal conditions (500 °C and visible light irradiation).

The results in Figure 5a,b reveal that with the increase in Nb_2O_5 proportion, the efficiency of Rh/Ga_xNb_y in thermal-driven DRM increased. Rh/Ga_0Nb_4 exhibited the highest catalytic activity with 226.4 and 205.1 $\mu mol \cdot g^{-1} \cdot min^{-1}$ of the initial CO_2 and CH_4 conversion rates, respectively. With the introduction of visible light, the efficiency of all the Rh/Ga_xNb_y catalysts was improved (Figure 5c,d). With the increase in Nb_2O_5 proportion in Rh/Ga_xNb_y, the ratios between photothermal catalytic activity and traditional thermal-driven catalytic activity also improved (they were 2.5, 1.7, 1.6, 1.4, and 1.4, respectively). In addition, the initial conversion rates of CO_2 and CH_4 over Rh/Ga_0Nb_4 were 578.0 $\mu mol \cdot g^{-1} \cdot min^{-1}$ and 504.0 $\mu mol \cdot g^{-1} \cdot min^{-1}$, respectively, which is 4.9 times higher than Rh/Ga_4Nb_0 (the initial conversion rates of CO_2 and CH_4 were 113.5 $\mu mol \cdot g^{-1} \cdot min^{-1}$ and 74.1 $\mu mol \cdot g^{-1} \cdot min^{-1}$, respectively). Significantly higher than conventional methane dry reforming catalysts (Table S1). The efficiency of Ga_xNb_y supports under photothermal DRM conditions was also tested. The experimental results show that Ga_xNb_y without the Rh active sites was almost inactive in the DRM reaction (Figure S5). In photothermal catalysis, the CO and H_2 yields of Rh/Ga_0N_4 were the highest and most stable, which were 362.9 $\mu mol \cdot g^{-1} \cdot min^{-1}$ and 221.9 $\mu mol \cdot g^{-1} \cdot min^{-1}$, respectively, and the yields of the other catalysts were attenuated, while in the thermocatalysis, the yields of all catalysts were lower and the attenuation was more significant (Figure S6). The CO_2 conversion of Rh/Ga_0Nb_4 (Figure S7a) was stable at about 27.2%, and the conversion of CH_4 (Figure S7b) was about 23.1%, which was significantly higher than that of the other catalysts. Compared with photothermal catalysis, the performance of all catalysts in thermal catalysis decreased, with the CO_2 conversion of about 10.6% for Rh/Ga_0Nb_4 and 9.5% for CH_4, while the conversion of the other catalysts was lower and slightly attenuated over time (Figure S7c,d).

Moreover, Rh/Ga_0N_4 has a relatively stable H_2/CO ratio (Figure S8). We tested the SEM of the catalyst after the 4 h photothermal DRM reaction, and the results show that Rh was still evenly distributed on the surface of the catalyst without aggregation. Moreover, although carbon was detected, the carbon element did not completely cover the active site on the catalyst surface, which proved that it has a certain ability to resist carbon deposition (Figure S9). The efficiency of the carrier without the active ingredient under photothermal DRM conditions was tested. The experimental results show that the carrier without the active ingredient was virtually inactive in the DRM reaction. This confirms the necessity of the active Rh component in driving photothermal DRM reactions. Moreover, Rh/Ga_xNb_y were stable in DRM. With the prolonged reaction time, the reaction activity was almost maintained. We tested the DRM measurements of the Rh/Ga_0Nb_4 catalyst under light conditions for 50 h (Figure S10) and it can be seen that the catalyst exhibits good stability over 50 h. In order to determine the contribution of light and heat to the reaction effect in the photothermal catalytic DRM reaction, we evaluated the activity of each catalyst under only light illumination conditions (Figure 5e,f). The results show that the activity of the Rh/Ga_xNb_y catalysts was very low, suggesting that the contribution of photothermal properties was more than optoelectronic properties [34–38].

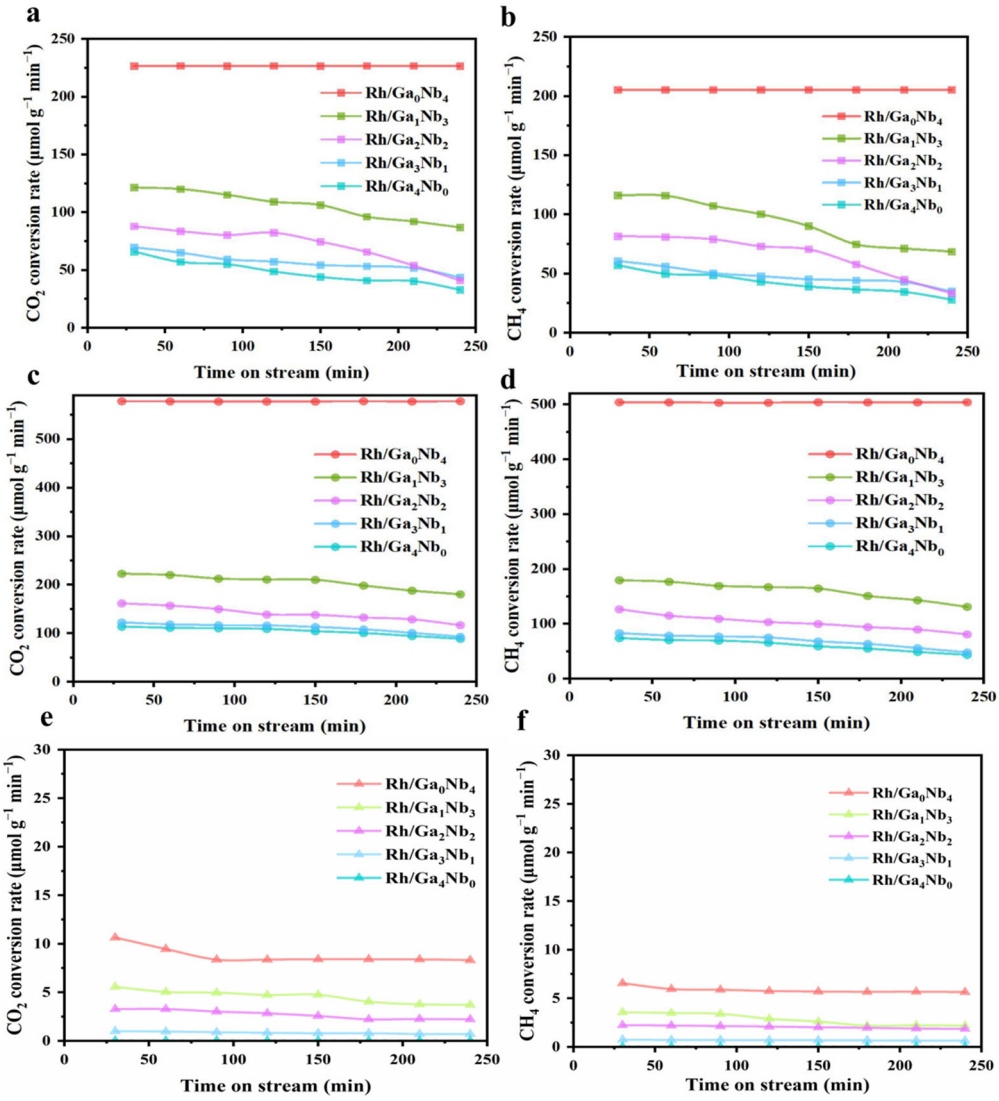

Figure 5. The thermal catalytic efficiency of Rh/Ga_xNb_y in the thermal-driven DRM reaction. (**a**) CO_2 conversion and (**b**) CH_4 conversion. Reaction conditions: 500 °C, CH_4:CO_2 = 1:1, total flow

rate: 10 mL·min^{-1}, 0.10 g of the Rh_2O_3/Ga_xNb_y catalyst, and without visible light irradiation. The photothermal catalytic efficiency of Rh/Ga_xNb_y in the photothermal DRM reaction system. (**c**) CO_2 conversion and (**d**) CH_4 conversion. Reaction conditions: 500 °C, CH_4:CO_2 = 1:1, total flow rate: 10 mL·min^{-1}, 0.10 g of the Rh_2O_3/Ga_xNb_y catalyst, with visible light irradiation (300 W Xe lamp, λ > 420 nm). Photocatalytic DRM efficiency of Rh/Ga_xNb_y under only light irradiation. (**e**) CO_2 conversion and (**f**) CH_4 conversion rates. Reaction conditions: CH_4:CO_2 = 1:1, total flow rate: 10 mL·min^{-1}, 0.10 g of the Rh_2O_3/Ga_xNb_y catalyst, and visible light irradiation (300 W Xe lamp, λ > 420 nm).

2.3. Property–Efficiency Relationship of Rh/Ga_xNb_y in DRM

By combining the above characterization results and the catalytic efficiency, it was discovered that (i) the catalytic efficiency of Rh/Ga_xNb_y in thermal-driven DRM is proportional to the amount of CO_2 desorption from β and γ peaks (Table 3 and Figure S11); (ii) the catalytic activity enhancement of Rh/Ga_xNb_y in DRM upon visible light irradiation (the activity enhancements were 2.5, 1.7, 1.6, 1.4, and 1.4, respectively, over Rh/Ga_0Nb_4, Rh/Ga_1Nb_3, Rh/Ga_2Nb_2, Rh/Ga_3Nb_1, and Rh/Ga_4Nb_0) is related to the number of electron–hole pairs available for photocatalytic reactions, as indicated by the photocurrent intensity in Table 4 (the photocurrent intensity is in the order of Rh/Ga_0Nb_4 > Rh/Ga_1Nb_3 > Rh/Ga_2Nb_2 > Rh/Ga_3Nb_1 > Rh/Ga_4Nb_0).

Table 4. The photothermal catalytic efficiency of Rh/Ga_xNb_y in photothermally driven DRM is related to the photocurrent intensity.

Sample	CO_2 Conversion Rate (μmol·g^{-1}·min^{-1})	Photocurrent Intensity (μA·cm^{-1})
Rh/Ga_0Nb_4	578.01	0.84
Rh/Ga_1Nb_3	222.26	0.67
Rh/Ga_2Nb_2	161.62	0.45
Rh/Ga_3Nb_1	122.15	0.35
Rh/Ga_4Nb_0	113.54	0.31

Based on the above results, the relationship between catalyst properties and catalytic behavior was determined. (i) In thermal-driven DRM, CO_2 activation could be considered as the rate-determining step since high energy is required for the activation of the stable nonpolar CO_2 molecules [39,40]. According to the literature, the medium and strong basic sites (β and γ peaks in CO_2-TPD) play important roles in accelerating the adsorption and activation of CO_2 through acid–base interactions [41,42]. Therefore, the larger amounts of medium and strong basic sites over Rh/Ga_xNb_y are beneficial for CO_2 activation and thus improved catalytic activity. The increasing ratio of Ga_2O_3 in Rh/Ga_xNb_y leads to more active sites, meaning that the reasonable control of the ratio of Ga_2O_3 and Nb_2O_5 is important to the catalytic activity. (ii) In addition to the effect from medium and strong basic sites, upon visible light irradiation, photoexcited charge carriers were generated and migrated to the catalyst surface to drive the DRM reaction. From this perspective, the presence of Rh-NPs is able to improve the charge transfer ability. Thus, the stronger photocurrent intensity further results in the higher catalytic DRM activity.

The exceptional photocatalytic activity of the Rh/Ga_0Nb_4 catalyst can be attributed to several key factors that synergistically enhance its performance. As shown in the UV-Vis absorption spectra and photocurrent experiments in Figure 4, the Rh/Ga_0Nb_4 catalyst exhibits significantly enhanced visible light absorption, indicating an expansion of its light absorption range. Simultaneously, the photocurrent results demonstrate a notable increase in the generation of photogenerated electron–hole pairs on the surface of the Rh/Ga_0Nb_4 catalyst under illumination, which effectively promotes the photocatalytic reaction process.

These factors collectively contribute to the remarkable improvement in the photocatalytic activity of the Rh/Ga_0Nb_4 catalyst. Furthermore, CO_2-TPD quantitative analysis reveals a significant enhancement in the CO_2 adsorption capacity of the Rh/Ga_0Nb_4 catalyst (Table 3). The improved CO_2 adsorption provides more reactants for the catalytic reaction, thereby further enhancing the catalytic activity.

In summary, the enhanced catalytic activity of the Rh/Ga_0Nb_4 catalyst can be primarily attributed to the following two aspects: (i) improved visible light absorption and increased concentration of photogenerated charge carriers; (ii) significant enhancement in CO_2 adsorption capacity. These improvements work synergistically, resulting in the superior catalytic efficiency of the Rh/Ga_0Nb_4 catalyst.

3. Experimental Section

3.1. Materials

Gallium oxide (Ga_2O_3, 99.99%) and Niobium(V) oxide (Nb_2O_5, 99.5%) were purchased from Aladdin and Sinopharm Chemical Reagent Co., Ltd., Shanghai, China, respectively. Deionized water (H_2O) and Rhodium (III) chloride hydrate ($RhCl_3 \cdot xH_2O$, 99.9%) were purchased from CNMC Shenyang Research Institute of Nonferrous Metals Co., Ltd., Shenyang, China.

3.2. Catalyst Preparation

Ga_2O_3-Nb_2O_5 supports were prepared by the physical mixing method. In a typical preparation procedure, 1.25 g of Ga_2O_3 and 3.75 g of Nb_2O_5 were weighed and mixed in a mortar to achieve different mass ratios. Specifically, the mass ratios of Ga_2O_3 to Nb_2O_5 were set as 0%, 25%, 50%, 75%, and 100%. Then, Ga_2O_3-Nb_2O_5 (x:y) was obtained, where x and y represent the proportions of Ga_2O_3 and Nb_2O_5, respectively.

The Rh_2O_3/Ga_2O_3-Nb_2O_5 (x:y) catalyst precursor was prepared by the following incipient wetness impregnation method: Take 0.10 g of Ga_2O_3-Nb_2O_5 (x:y) support and put it into a 100 mL beaker. Measure a certain amount of $RhCl_3 \cdot xH_2O$ aqueous solution and pour it into the beaker; then, add 30 mL of distilled water. The mixture was continuously stirred at room temperature for 12 h, followed by evaporation at 100 °C with constant agitation until complete H_2O removal. Then, the substance was dried overnight at 80 °C in an oven and calcined in a muffle furnace at 550 °C for 4 h under an air atmosphere (heating rate: 2 °C/min). The theoretical loading amounts of Rh on Rh_2O_3/Ga_2O_3-Nb_2O_5 (x:y) were 1.0 wt%.

Rh_2O_3/Ga_2O_3-Nb_2O_5 (x:y) was further reduced in 10% H_2/Ar at 500 °C for 2 h to obtain a partially reduced catalyst, which was denoted as Rh/Ga_xNb_y. In addition, the Rh_2O_3/Ga_2O_3-Nb_2O_5 (x:y) consumed after DRM evaluation was also recorded as Rh/Ga_xNb_y.

3.3. Catalyst Characterizations

The structure and phase analysis of fresh and spent catalysts were performed on a Bruker D8 Advance X-ray Diffractometer (XRD) (Rigaku, Kyoto, Japan), using Ni-filtered Cu radiation and instrumental settings of 40 kV and 40 mA. The characterization conditions are a scanning angle of 10–80°, a scanning speed of 5° min^{-1}, and a scanning step of 0.02°.

The specific surface area and pore structure were measured by N_2 adsorption–desorption with the Brunauer–Emmett–Teller (BET) method on a Micromeritics ASAP 2020 C analyzer (Micromeritics, Norcross, GA, USA). Before measurements, the samples were degassed at 200 °C for 2 h.

The valence states of elements on the catalyst surface were analyzed on an Agilent 5100 X-ray photoelectron spectroscopy (XPS) (Agilent Technologies, Dallastown, PA, USA).

The basic operating parameters were as follows: tube voltage of 15 kV, tube current of 10 mA, test energy of Al target of 1486.8 eV, and test spot diameter of 500 μm. The obtained data are calibrated based on the binding energy of C1s (284.8 eV).

The reducibility of oxide precursors was specifically investigated by H_2-temperature programmed reduction (H_2-TPR) on an AutoChem II 2930 chemical adsorption instrument (Micromeritics, Norcross, GA, USA). Typically, 50 mg samples were pretreated by N_2 at 300 °C for 1 h. After cooling to room temperature, the pretreated samples were heated at a rate of 10 °C·min^{-1} to 800 °C in 10% H_2/Ar. The signals were recorded by a thermal conductivity detector.

The morphology of catalysts was observed using a transmission electron microscope (TEM-16-TS-008, Thermo Fisher Scientific, Waltham, MA, USA). Prior to imaging, the sample was sonicated and dispersed in ethanol and then deposited on a copper TEM grid.

The basic properties of the catalysts were characterized by CO_2-temperature programmed desorption (CO_2-TPD) on an AutoChem III 2930 chemical adsorption instrument (Micromeritics, Norcross, GA, USA). An amount of 100 mg of the sample was firstly pretreated by He at a gas flow rate of 30 mL min^{-1} at 300 °C for 1 h and then cooled to 50 °C. Subsequently, a 10% CO_2/He (30 mL min^{-1}) mixture was introduced and continuously adsorbed for 1 h until saturation, which can be determined by monitoring the concentration of the outgoing gas. As the adsorption sites on the material surface are gradually occupied by CO_2, the unadsorbed CO_2 will flow out of the reactor along with the carrier gas. When the concentration of CO_2 at the outlet tends to be consistent with that at the inlet, it indicates that the adsorption has reached dynamic equilibrium (saturation). After that, He gas was switched to remove residual CO_2 physically adsorbed on the catalyst surface. Finally, under the He atmosphere, the temperature was raised from 50 °C to 800 °C at a rate of 10 °C min^{-1}, and the effluent gas was detected using a thermal conductivity detector.

The light-harvesting capacity of the catalysts was characterized by a UV-3600 UV visible diffuse reflectance spectroscopy, with a wavelength range of 200–800 nm on a Japanese Shimadzu UV-3600i Plus Spectrometer.

3.4. Photoelectrochemical (PEC) Measurement

The photocurrents of the catalysts were tested on a DH7000 electrochemical workstation (Shanghai Chenhua Instrument Co., Ltd., Shanghai, China). The photoanode film was prepared as follows: 5.0 mg portion of Rh/Ga_xNb_y and 5.0 mL of anhydrous ethanol were mixed and ultra-sounded for 30 min to evenly disperse Rh/Ga_xNb_y in ethanol without precipitation. The suspension (approximately 5.5 mL) was then dropped onto a fluorine-doped tin oxide conductive layer to obtain the photoanode film. The experiment was conducted using a CHI600E series electrochemical workstation. Connected to the electrochemical workstation with a three-electrode quartz glass cell. The setup employed platinum wire as the counter electrode, an Ag/AgCl electrode as the reference electrode, and the prepared photocathode as the working electrode. The photoelectrochemical efficiency of different photocathode film samples was tested under irradiation of a 300 W Xe lamp in a 0.5 M potassium sulfate (K_2SO_4) aqueous solution. The detection principle involves utilizing the three-electrode system and the electrolyte solution to form an external circuit, through which transient photocurrent curves are measured by applying a constant bias as shown in Figure S12.

3.5. Catalyst Evaluation

The DRM reaction was conducted in a fixed-bed reactor under atmospheric pressure. An amount of 0.10 g of catalyst was uniformly dispersed in the constant zone of a quartz tube reactor. Both heat (500 °C) and a 300 W Xe lamp with L42 filter ($\lambda > 420$ nm) were

employed to provide the energy input. High-purity CH_4 and CO_2 with a molar ratio of 1/1 were introduced into the reactor with a total flow rate of 10.0 mL·min^{-1} (STP). The catalyst was kept at each temperature for 30 min. Then, the composition of the outlet gas was analyzed by an online gas chromatograph equipped with a TCD. The chromatograph is an SP-6890 gas chromatograph. The size of the column is 3 m × 3 mm, and the column temperature is 50 °C. Furthermore, the flow rate of the effluent gas was measured with a flowmeter. To investigate the differences between photothermal catalysis and traditional thermal catalysis, a separate thermal catalysis experiment was conducted. The efficiency evaluation process was consistent with the aforementioned method, except that no light irradiation was applied. The reaction temperature was precisely measured by using thermocouples. The test results are shown in Table 5 as follows:

Table 5. The DRM actual reaction process temperature.

Catalysts	Set the Temperature (°C)	Actual Reaction Process Temperature (°C)	
		Photothermal	Thermal
Rh/Ga_0Nb_4	500	483.5	490.2
Rh/Ga_1Nb_3	500	483.3	491.3
Rh/Ga_2Nb_2	500	484.6	490.8
Rh/Ga_3Nb_1	500	484.2	491.7
Rh/Ga_4Nb_0	500	483.9	490.6

4. Conclusions

In this study, Rh/Ga_xNb_y was prepared as a model catalyst through an in situ reduction strategy to elucidate the structure–efficiency relationship of reducible oxide-supported photothermal catalysts containing group VIII metals. H_2-TPR and XPS analyses confirmed that Rh/Ga_xNb_y served as an intrinsic catalyst in the DRM reaction. CO_2-TPD and photocurrent characterizations revealed that the CO_2 adsorption capacity and the separation efficiency of photogenerated electron–hole pairs gradually improved with increasing Nb_2O_5 content. The optimal catalyst Rh/Ga_0Nb_4 exhibited initial conversion rates of 578.0 μmol·g^{-1}·min^{-1} for CO_2 and 504.0 μmol·g^{-1}·min^{-1} for CH_4. Based on the characterization results and photothermal catalytic efficiency, the following structure–efficiency relationships were established: (i) the catalytic efficiency of Rh/Ga_xNb_y in thermally driven DRM is correlated with the number of medium-strong basic sites on its surface, which can be modulated by the ratio of Ga_2O_3 to Nb_2O_5 supports; (ii) the visible light-induced activity enhancement is related to the quantity of electron–hole pairs available for photocatalytic reactions, while Rh nanoparticles further improve charge transfer efficiency. Therefore, this work not only provides a facile in situ reduction strategy for constructing photothermal composite catalysts but also offers theoretical guidance for designing efficient photothermal catalysts for DRM applications.

Supplementary Materials: The following supporting information can be downloaded at: https://www.mdpi.com/article/10.3390/catal15040312/s1, Figure S1: H_2-TPR results of Ga_2O_3-Nb_2O_5 precursors.; Figure S2. TEM and HR-TEM images.Figure S3. UV-vis spectra of Ga_xNb_y catalysts. Figure S4.; Tauc plots and bandgap of Rh/Ga_xNb_y catalysts.; Figure S5. Photothermal catalytic efficiency of Ga_xNb_y in photothermal DRM reaction system.; Figure S6. Photothermal catalytic efficiency of Rh/Ga_xNb_y in photothermal DRM reaction system. (a) CO yield and (b) H_2 yield.; Figure S7. Photothermal catalytic efficiency of Rh/Ga_xNb_y in photothermal DRM reaction system. (a) CO_2 conversion and (b) CH_4 conversion.; Figure S8. H_2/CO ratio over all catalysts.; Figure S9. SEM image and EDX mapping of the catalyst after 4 h of photothermal DRM reaction.; Figure S10. Photothermal catalytic efficiency of Rh/Ga_xNb_y in photothermal DRM reaction system.; Figure S11. The catalytic

efficiency of Rh/Ga_xNb_y in thermally driven DRM is related to the CO_2 desorption capacity of the β and γ peaks.; Figure S12. Photoelectrochemical efficiency evaluation system.; Table S1: Comparison table of thermal and photothermal catalysts for DRM reactions. References [11–13,43–48] are cited in the Supplementary Materials.

Author Contributions: Y.L. (Yuqiao Li): methodology, validation; S.S.: formal analysis, writing—original draft; D.L.: formal analysis, writing—review and editing; H.L. (corresponding author): supervision, validation; Y.L. (Yiming Lei) (corresponding author): supervision, validation. All authors have read and agreed to the published version of the manuscript.

Funding: This work received financial support from the Young Talent Plan of Liaoning Province (XLYC2203068), the Scientific Research Foundation of Technology Department of Liaoning Province of China (2022-MS-379), and the National Natural Science Foundation of China (21902116).

Data Availability Statement: The data presented in this study are available upon request from the corresponding authors.

Conflicts of Interest: The authors declare no conflicts of interest.

References

1. Oertel, C.; Matschullat, J.; Zurba, K.; Zimmermann, F.; Erasmi, S. Greenhouse gas emissions from soils—A review. *Geochemistry* **2016**, *76*, 327–352.
2. Kolle, J.M.; Fayaz, M.; Sayari, A. Understanding the effect of water on CO_2 adsorption. *Chem. Rev.* **2021**, *121*, 7280–7345. [PubMed]
3. Liu, H.; Song, H.; Zhou, W.; Meng, X.; Ye, J. A promising application of optical hexagonal Tan in photocatalytic reactions. *Angew. Chem. Int. Edit.* **2018**, *57*, 16781–16784.
4. Liu, H.; Meng, X.; Dao, T.D.; Liu, L.; Li, P.; Zhao, G.; Nagao, T.; Yang, L.; Ye, J. Light assisted CO_2 reduction with methane over SiO_2 encapsulated Ni nanocatalysts for boosted activity and stability. *J. Mater. Chem. A* **2017**, *5*, 10567–10573.
5. Wang, C.; Qiu, Y.; Zhang, X.; Zhang, Y.; Sun, N.; Zhao, Y. Geometric design of a Ni@silica nano-capsule catalyst with superb methane dry reforming stability: Enhanced confinement effect over the nickel site anchoring inside a capsule shell with an appropriate inner cavity. *Catal. Sci. Technol.* **2018**, *8*, 4877–4890.
6. Bu, K.; Deng, J.; Zhang, X.; Kuboon, S.; Yan, T.; Li, H.; Shi, L.; Zhang, D. Promotional effects of B-terminated defective edges of Ni/boron nitride catalysts for coking- and sintering-resistant dry reforming of methane. *Appl. Catal. B-Environ.* **2020**, *267*, 118692.
7. Yao, J.-L.; Zheng, H.-Y.; Bai, P.-W.; Liang, W.-P.; Zhang, Z.-Y.; Li, T.; Xie, T. Design and optimization of solar-dish volumetric reactor for methane dry reforming process with three-dimensional optics-CFD method. *Energ. Convers. Manag.* **2023**, *277*, 116663.
8. Kim, W.Y.; Lee, Y.H.; Park, H.; Choi, Y.H.; Lee, M.H.; Lee, J.S. Coke tolerance of Ni/Al_2O_3 nanosheet catalyst for dry reforming of methane. *Catal. Sci. Technol.* **2016**, *6*, 2060–2064.
9. Cho, Y.; Shoji, S.; Yamaguchi, A.; Hoshina, T.; Fujita, T.; Abe, H.; Miyauchi, M. Visible-light-driven dry reforming of methane using a semiconductor-supported catalyst. *Chem. Commun.* **2020**, *56*, 4611–4614.
10. Zhang, N.; Han, C.; Fu, X.; Xu, Y.-J. Function-Oriented engineering of Metal-Based nanohybrids for photoredox catalysis: Exerting plasmonic effect and beyond. *Chem* **2018**, *4*, 1832–1861.
11. Liu, H.; Meng, X.; Dao, T.D.; Zhang, H.; Li, P.; Chang, K.; Wang, T.; Li, M.; Nagao, T.; Ye, J. Conversion of carbon dioxide by methane reforming under Visible-Light irradiation: Surface-Plasmon-Mediated nonpolar molecule activation. *Angew. Chem. Int. Edit.* **2015**, *54*, 11545–11549.
12. Song, H.; Meng, X.; Dao, T.D.; Zhou, W.; Liu, H.; Shi, L.; Zhang, H.; Nagao, T.; Kako, T.; Ye, J. Light-Enhanced carbon dioxide activation and conversion by effective plasmonic coupling effect of Pt and Au nanoparticles. *ACS Appl. Mater. Inter.* **2018**, *10*, 408–416.
13. Liu, H.; Li, M.; Dao, T.D.; Liu, Y.; Zhou, W.; Liu, L.; Meng, X.; Nagao, T.; Ye, J. Design of PdAu alloy plasmonic nanoparticles for improved catalytic performance in CO_2 reduction with visible light irradiation. *Nano Energy* **2016**, *26*, 398–404.
14. Hou, Z.; Chen, P.; Fang, H.; Zheng, X.; Yashima, T. Production of synthesis gas via methane reforming with CO_2 on noble metals and small amount of noble-(Rh-) promoted Ni catalysts. *Catal. Sci. Technol.* **2006**, *31*, 555–561.
15. Hassan, N.E.; Kaydouh, M.N.; Geagea, H.; Zein, H.E.; Jabbour, K.; Casale, S.; Zakhem, H.E.; Massiani, P. Low temperature dry reforming of methane on rhodium and cobalt based catalysts: Active phase stabilization by confinement in mesoporous SBA-15. *Appl. Catal. A-Gen.* **2016**, *520*, 114–121.
16. Li, Y.; Li, D.; Liu, H.; Lei, Y.; Zhao, R.; He, D.; Zheng, Z.; Luo, H.; Liu, A. In situ fabricating a Rh/Ga_2O_3 photothermal catalyst for dry reforming of methane. *Catal. Sci. Technol.* **2024**, *14*, 2722.

17. Liu, H.; Meng, X.; Yang, W.; Zhao, G.; He, D.; Ye, J. Photo-thermal CO_2 reduction with methane on group VIII metals: In situ reduced WO_3 support for enhanced catalytic activity. *Chin. J. Catal.* **2021**, *42*, 1976–1982.
18. Li, Y.; Guo, J.; Liu, H.; Liu, A.; Li, D. In situ generated oxygen vacancy on Nb_2O_5 for boosted catalytic activities of M/Nb_2O_5 in photothermal CO_2 reforming of CH_4. *J. CO2 Util.* **2023**, *67*, 102330.
19. Kim, Y.; Kang, S.; Kang, D.; Lee, K.R.; Song, C.K.; Sung, J.; Kim, J.S.; Lee, H.; Park, J.; Yi, J. Single-Phase formation of Rh_2O_3 nanoparticles on h-BN support for highly controlled methane partial oxidation to syngas. *Angew. Chem. Inter. Edit.* **2021**, *60*, 25411–25418.
20. Bueno-López, A.; Such-Basáñez, I.; Lecea, C.S.-M.d. Stabilization of active Rh_2O_3 species for catalytic decomposition of N_2O on La-, Pr-doped CeO_2. *J. Catal.* **2006**, *244*, 102–112.
21. Suzuki, H.; Takashima, T.; Tomita, O.; Kanazawa, T.; Nozawa, S.; Kato, K.; Yamakata, A.; Nakashima, K.; Saeki, A.; Abe, R. Improved photocatalytic O_2 evolution on a Sillén–Aurivillius perovskite oxychloride $Bi_6NBWO_{14}Cl$ by Rh_2O_3 additives and surface modifications. *J. Phy Chem. C* **2023**, *127*, 7965–7973.
22. Nakayama, H.; Nagata, M.; Tomie, T.; Ishitsuka, T.; Matsubayashi, N.; Shimizu, Y. Strong Metal–Support interaction mechanisms of Rh supports in the CO–NO reaction: Rh/Rh_2O_3 interconversion in promoting NO dissociation and CO_2 generation. *J. Phy Chem. C* **2022**, *126*, 17904–17912.
23. Dou, L.; Liu, Y.; Gao, Y.; Li, J.; Hu, X.; Zhang, S.; Ostrikov, K.K.; Shao, T. Disentangling metallic cobalt sites and oxygen vacancy effects in synergistic plasma-catalytic CO_2/CH_4 conversion into oxygenates. *Appl. Catal. B-Environ.* **2022**, *318*, 121830.
24. Zhang, Q.; Yang, P.; Zhang, H.; Zhao, J.; Shi, H.; Huang, Y.; Yang, H. Oxygen vacancies in Co_3O_4 promote CO_2 photoreduction. *Appl. Catal. B-Environ.* **2022**, *300*, 120729.
25. Xu, Q.; Zhang, S. Fabrication and photoluminescence of B-Ga_2O_3 nanorods. *Superlattice Microst.* **2008**, *44*, 715–720.
26. Liu, H.; Wang, Z.; Li, H.; Zhang, X.; Qin, X.; Dai, Y.; Wang, P.; Liu, Y.; Huang, B. Photocatalytic degradation of ethylene by Ga_2O_3 polymorphs. *RSC Adv.* **2018**, *8*, 14328–14334.
27. Kulkarni, A.K.; Praveen, C.S.; Sethi, Y.A.; Panmand, R.P.; Arbuj, S.S.; Naik, S.D.; Ghule, A.V.; Kale, B.B. Nanostructured N-doped orthorhombic Nb_2O_5 as an efficient stable photocatalyst for hydrogen generation under visible light. *Dalton T.* **2017**, *46*, 14859–14868.
28. Hao, W.; Wang, Z.; Xie, S.; Wei, L.; Hou, Z.; Liu, Y.; Dai, H.; Deng, J. Catalytic performance of Nb_2O_5 modified Ru/CeO_2 for dichloromethane oxidation. *Prog. Nat. Sci.* **2023**, *33*, 486–494.
29. Hou, H.; Yang, W.; Sun, H.; Zhang, H.; Feng, X.; Kuang, Y. Tailored synthesis of Ga_2O_3 nanofibers towards enhanced photocatalytic hydrogen evolution. *Catal. Lett.* **2023**, *153*, 2950–2958.
30. Boukha, Z.; Gil-Calvo, M.; Rivas, B.d.; González-Velasco, J.R.; Gutiérrez-Ortiz, J.I.; López-Fonseca, R. Behaviour of Rh supported on hydroxyapatite catalysts in partial oxidation and steam reforming of methane: On the role of the speciation of the Rh particles. *Appl. Catal. A-Gen.* **2018**, *556*, 191–203.
31. Han, F.; Liu, H.; Cheng, W.; Xu, Q. Highly selective conversion of CO_2 to methanol on the CuZnO–ZrO_2 solid solution with the assistance of plasma. *RSC Adv.* **2020**, *10*, 33620–33627. [PubMed]
32. Qi, S.-C.; Wu, J.-K.; Lu, J.; Yu, G.-X.; Zhu, R.-R.; Liu, Y.; Liu, X.-Q.; Sun, L.-B. Underlying mchanism of CO_2 adsorption onto conjugated Azacyclo-copolymers: N-doped adsorbents capture CO_2 chiefly through Acid–Base interaction? *J. Mater. Chem. A* **2019**, *7*, 17842–17853.
33. Shang, B.; Zhao, F.; Choi, C.; Jia, X.; Pauly, M.; Wu, Y.; Wang, H. Monolayer molecular functionalization enabled by Acid–Base interaction for High-Performance photochemical CO_2 reduction. *ACS Energy Lett.* **2022**, *7*, 2265–2272.
34. Guo, C.; Tang, Y.; Yang, Z.; Zhao, T.; Liu, J.; Zhao, Y.; Wang, F. Reinforcing the efficiency of photothermal catalytic CO_2 methanation through integration of Ru nanoparticles with photothermal $MnCo_2O_4$ nanosheets. *ACS Nano* **2023**, *17*, 23761–23771.
35. Yang, Z.; Zhao, T.; Hao, S.; Wang, R.; Zhu, C.; Tang, Y.; Guo, C.; Liu, J.; Wen, X.; Wang, F. Large-Scale synthesis of multifunctional Single-phase Co_2C nanomaterials. *Adv. Sci.* **2023**, *10*, 2301073.
36. Tang, Y.; Zhao, T.; Han, H.; Yang, Z.; Liu, J.; Wen, X.; Wang, F. Ir-Coo active centers supported on porous Al_2O_3 nanosheets as efficient and durable Photo-Thermal catalysts for CO_2 conversion. *Adv. Sci.* **2023**, *10*, 2300122.
37. Tang, Y.; Wang, H.; Guo, C.; Yang, Z.; Zhao, T.; Liu, J.; Wang, F. Ruthenium–Cobalt Solid-Solution Alloy nanoparticles for enhanced photopromoted thermocatalytic CO_2 hydrogenation to methane. *ACS Nano* **2024**, *18*, 11449–11461.
38. Yang, Z.; Zhao, T.; Tang, Y.; Jiang, Y.; Kitagawa, H.; Wen, X.; Wang, F. Size-Modulated Photo-Thermal catalytic CO_2 hydrogenation prformances over Pd nanoparticles. *J. Catal.* **2023**, *424*, 22–28.
39. Lu, Y.; Kang, L.; Guo, D.; Zhao, Y.; Zhao, Y.; Wang, S.; Ma, X. Double-Site doping of a V promoter on Ni_x-V-Mgal catalysts for the drm reaction: Simultaneous effect on CH_4 and CO_2 activation. *ACS Catal.* **2021**, *11*, 8749–8765.
40. Li, T.; Liang, Z.; Liu, J.; Zhang, Y.; Zhang, X.; Zhang, G. The role of cerium in cola bimetallic catalysts: Enhancing activation of CH_4 and CO_2 for improved drm reaction. *Int. J. Hydrogen Energy* **2024**, *61*, 611–622.
41. Shao, L.; Liu, M.; Sang, Y.; Zhan, P.; Chen, J.; Huang, J. Nitrogen-Doped ultrahigh microporous carbons derived from two Nitrogen-containing Post-Cross-Linked polymers for efficient CO_2 capture. *J. Chem. Eng. Data.* **2020**, *65*, 2238–2250.

42. Jin, S.; Guan, X.; Zhang, X.; Zhang, C.; Liu, J.; Wang, Y.; Wang, Y.; Li, R.; Li, Z.; Fan, C. CeO_2 nanorods with bifunctional oxygen vacancies for promoting Low-Pressure photothermocatalytic CO_2 conversion with CH_3OH to dimethyl carbonate. *J. Environ. Chem. Eng.* **2023**, *11*, 111374.
43. Ji, G.; Wu, S.; Song, X.; Meng, L.; Jia, Y.; Tian, J. Recent progress in Photo-Thermal synergistic catalysis for methane dry reforming. *Int. J. Hydrogen Energy* **2024**, *57*, 696–708.
44. Yabe, T.; Yamada, K.; Murakami, K.; Toko, K.; Ito, K.; Higo, T.; Ogo, S.; Sekine, Y. Role of electric field and surface protonics on Low-Temperature catalytic dry reforming of methane. *ACS Sustain. Chem. Eng.* **2019**, *7*, 5690–5697.
45. Song, Z.; Wang, Q.; Guo, C.; Li, S.; Yan, W.; Jiao, W.; Qiu, L.; Yan, X.; Li, R. Improved effect of Fe on the stable $NiFe/Al_2O_3$ catalyst in Low-Temperature dry reforming of methane. *Ind. Eng. Chem. Res.* **2020**, *59*, 17250–17258.
46. Lorber, K.; Zavašnik, J.; Arčon, I.; Huš, M.; Teržan, J.; Likozar, B.; Djinović, P. CO2 activation over nanoshaped CeO_2 decorated with nickel for Low-Temperature methane dry reforming. *ACS Appl. Mater. Inter.* **2022**, *14*, 31862–31878.
47. Ramon, A.P.; Li, X.; Clark, A.H.; Safonova, O.V.; Marcos, F.C.; Assaf, E.M.; Bokhoven, J.A.v.; Artiglia, L.; Assaf, J.M. In Situ study of Low-Temperature dry reforming of methane over $La_2Ce_2O_7$ and $LaNiO_3$ mixed oxides. *Appl. Catal. B-Environ.* **2022**, *315*, 121528.
48. Ballesteros-Plata, D.; Infantes-Molina, A.; Rodríguez-Castellón, E.; Cauqui, M.A.; Yeste, M.P. Improving noble metal catalytic activity in the dry reforming of methane by adding niobium. *Fuel* **2022**, *308*, 121996.